

VISUALISATION OF SPHERICAL HARMONICS IN PEIRCE'S QUINCUNCIAL PROJECTION

BJÖRN MALTE SCHÄFER ^{1,2}[✉]¹ Zentrum für Astronomie der Universität Heidelberg, Astronomisches Rechen-Institut, Philosophenweg 12, 69120 Heidelberg, Germany and² Interdisziplinäres Zentrum für wissenschaftliches Rechnen, Universität Heidelberg, INF205, 69120 Heidelberg, Germany

Version January 27, 2026

Abstract

The spherical harmonics $Y_{\ell m}(\theta, \varphi)$ are complex-valued functions on the surface of a sphere, and have found widespread application in physics and astronomy. Every physics students knows them from quantum mechanics and electromagnetic theory, where they form the basis of hydrogen orbitals and of the multipole expansion, respectively. More advanced applications include the physics of the cosmic microwave background, gravitational lensing, and gravitational waves. In this paper I aim to contrast their usual 3d visualisation with Peirce's quincuncial projection, a conformal projection of the sphere onto a 2d unfolded square dihedron, where the projection respects the fundamental rotational symmetries and preserves angles. With this mapping, I guide the reader through the properties of the spherical harmonics in a pedagogical way and show that many of their mathematical relations have an intuitive visualisation on Peirce's 2d map, which might be useful for people challenged by processing 3d shapes, or which people might appreciate aesthetically.

Keywords: visualisation, map projections, spherical harmonics

1. INTRODUCTION: SPHERICAL HARMONICS $Y_{\ell m}(\theta, \varphi)$ 1.1. *A harmonic system on the sphere*

The spherical harmonics solve the differential equation

$$\Delta Y_{\ell m}(\theta, \varphi) = -\ell(\ell + 1)Y_{\ell m}(\theta, \varphi), \quad (1)$$

with integer $\ell \geq 0$ and with the boundary condition $Y_{\ell m}(\theta, \varphi + 2\pi) = Y_{\ell m}(\theta, \varphi)$, where Δ is the Laplace-operator on the sphere,

$$\Delta = \frac{1}{\sin \theta} \frac{\partial}{\partial \theta} \left(\sin \theta \frac{\partial}{\partial \theta} \right) + \frac{1}{\sin^2 \theta} \frac{\partial^2}{\partial \varphi^2}, \quad (2)$$

with the azimuthal angle φ and the polar angle θ . Because eqn. (1) is essentially the Helmholtz-differential equation, it provides a system of waves with wave number ℓ (and correspondingly, wave length $\lambda = \pi/\ell$ on the surface of the sphere. A separation ansatz $Y_{\ell m}(\theta, \varphi) = T(\theta) \times P(\varphi)$ leads to the explicit solution

$$Y_{\ell m}(\theta, \varphi) = \sqrt{\frac{2\ell + 1}{4\pi}} \sqrt{\frac{(\ell - m)!}{(\ell + m)!}} P_{\ell m}(\cos \theta) \exp(im\varphi) \quad (3)$$

in terms of associated Legendre-polynomials $P_{\ell m}(\cos \theta)$, and a complex phase $\exp(im\varphi)$. Solving eqn. (1) requires ℓ to be a positive integer, and m to be integer bounded by the condition $-\ell \leq m \leq +\ell$. Intuitively, the $Y_{\ell m}(\theta, \varphi)$ are waves in the azimuthal direction φ , and the amplitude is modulated through by the polynomials $P_{\ell m}(\cos \theta)$ with the polar angle θ .

The spherical harmonics $Y_{\ell m}(\theta, \varphi)$ are an orthonormal system of waves on the surface of the sphere, and allow the spectral decomposition in analogy to the Fourier-transform

$$\psi_{\ell m} = \int_{4\pi} d\Omega \psi(\theta, \varphi) Y_{\ell m}^*(\theta, \varphi) \quad (4)$$

[✉] bjoern.malte.schaefer@uni-heidelberg.de

with the solid angle element $d\Omega = \sin \theta d\theta d\varphi = d\cos \theta d\varphi$ for integration. The inverse operation is given by

$$\psi(\theta, \varphi) = \sum_{\ell=0}^{\infty} \sum_{m=-\ell}^{+\ell} \psi_{\ell m} Y_{\ell m}(\theta, \varphi). \quad (5)$$

There are numerically very efficient algorithms for computing these transforms, even in the limit of high ℓ , where the transform kernel is highly oscillatory, for instance the HEALPix-software used in data analysis of the cosmic microwave background (Gorski et al 1999, 2005). Generalisations of $Y_{\ell m}(\theta, \varphi)$ to non-scalar functions include the spin spherical harmonics ${}_s Y_{\ell m}(\theta, \varphi)$ (Goldberg et al 1967; Huffenberger and Wandelt 2010; Dray 1985), the spinor spherical harmonics for fermionic wave functions in relativistic quantum mechanics, and spin spheroidal harmonics if the condition of spherical symmetry is relaxed and functions defined on the surface of ellipsoids are considered (Hughes 2000).

1.2. *Applications in physics*

There is a plethora of applications in physics for the spherical harmonics: They appear in the multipole expansion of charge distributions ρ in electrodynamics for solving potential problems of the Poisson-type,

$$\Delta \Phi = -4\pi\rho, \quad (6)$$

in a convenient series with terms proportional to $1/r^{\ell+1}$ for the multipole contribution at order ℓ , with r being the distance of the observer to the charge distribution. In quantum mechanics, they appear naturally when solving the Schrödinger equation for spherically symmetric potentials $\Phi(r)$,

$$\left(-\frac{\hbar^2}{2m} \Delta + \Phi(r) \right) \psi = E\psi, \quad (7)$$

as exemplified by the hydrogen orbitals. More advanced applications include geophysics (Hudson 1978) and data analysis of the cosmic microwave background, whose fluctuation pattern on the celestial sphere is conveniently decomposed in terms of spherical harmonics by virtue of eqn. (4) (Maino et al 1999; Lewis and Challinor 2007; Leistedt et al 2015). Likewise in cosmology, full-sky analysis of the gravitational lensing effect is described using spherical harmonics, (Hanson et al 2010; Hirata and Seljak 2003; Beck et al 2018; Zaldarriaga and Seljak 1998; Seljak 1996; Nishizawa et al 2008; Okamoto and Hu 2003). Extensions like the spin-spherical harmonics have been constructed to deal with non-scalar fields such as polarisation of the cosmic microwave background, the cosmic gravitational wave background or the galaxy ellipticity field, (Fernández-Cobos et al 2016; Kamionkowski and Kovetz 2015; Gluscevic et al 2009; Adamek et al 2015; Hall and Taylor 2014; Merkel and Schaefer 2011). A comprehensive references of properties of the spherical harmonics $Y_{\ell m}(\theta, \varphi)$ is, for instance, Olver et al (2025).

2. VISUALISATION OF THE SPHERICAL HARMONICS

Visualisation of the spherical harmonics $Y_{\ell m}(\theta, \varphi)$ needs to take care of the fact that they are complex-valued, and that the topology of their domain is the sphere, i.e. they provide a mapping $\mathbb{S}^2 \rightarrow \mathbb{C}$, or equivalently, $\mathbb{S}^2 \rightarrow \mathbb{R}^2$. 3d-visualisations often suffer from that fact that foreground structures cover details further in the back: This is the motivation behind this article, which illustrates properties of spherical harmonics in Peirce's quincuncial projection. There, the full solid angle is mapped onto a square, such that all details of the $Y_{\ell m}(\theta, \varphi)$ are visible, irrespective of their localisation on the sphere.

One straightforward way of visualising the complex-valued spherical harmonics is computing their absolute value $|Y_{\ell m}(\theta, \varphi)|^2 = Y_{\ell m}(\theta, \varphi)Y_{\ell m}^*(\theta, \varphi)$ and to depict this value as the distance of a surface to the origin in spherical coordinates. Alternatively, one could resort to plotting real or imaginary values: Because of the oscillatory behaviour of $\exp(im\varphi) = \cos(m\varphi) + i\sin(m\varphi)$ one directly sees the variation in the azimuthal direction determined by the choice of m : One encounters m maxima and m minima in one circumnavigation in φ at fixed θ : The resulting visualisation directly corresponds to the atomic orbitals known from theoretical chemistry. In fact, solving the Schrödinger equation for obtaining the wave function of an electron in the Coulomb-field of an atomic nucleus would show that it comes out proportional to $Y_{\ell m}(\theta, \varphi)$ where the indices ℓ and m acquire the interpretation of quantum numbers. They indicate the magnitude of angular momentum and its orientation, and can be measured through the magnetic moment that is associated with the wave function of an electrically charged particle.

Phase information can be conveyed by the colouring, i.e. by cycling through the spectrum of the rainbow colours as the phase evolves from 0 to 2π . In many visualisations, this information is discarded. Instead, only positive and negative values of a real-numbered representation are given. The hue of the colouring can indicate the modulus of the complex numbers, for instance dimming the shade of colour towards black could indicate small values for $|Y_{\ell m}(\theta, \varphi)|$.

Common visualisations of the spherical harmonic function $Y_{43}(\theta, \varphi)$ are shown in Fig. 1 in 3d, in terms of absolute value, real value and phase. Clearly, not all information is

accessible, for instance the values of the complex phase on the far side of the spherical harmonic.

3. PEIRCE'S QUINCUNCIAL PROJECTION

Peirce's quincuncial projection is a conformal map projection from the sphere to an unfolded square dihedron, developed by C.S. Peirce (Peirce 1879). Each octant projects onto an isosceles triangle. Four of these are arranged into a diamond shape representing the Northern hemisphere, and the four remaining Southern hemisphere tiles can be added in a way to complete the diamond to a square. As such, the square forms a seamless tiling of the plane.

The projection proceeds in two steps: (i) a stereographic projection from the surface of a sphere onto a tangential plane, followed by (ii) a compactification onto the domain $[-1, +1] \otimes [-1, +1]$, where the latter is a ingenious application of Riemann's mapping theorem, due to (Schwarz 1869) and (Christoffel 1867), expertly explained by Driscoll and Trefethen (2002). The mapping theorem states that there is a bijective, holomorphic mapping between any open, simply-connected subset of the complex plane onto the open unit disc. As a special case, Schwarz and Christoffel constructed mappings between the unit disc and regular polygons, with the particular case of a square. This mapping is conformal except at four singular, isolated points along the equator. Otherwise, in particular on the X-shaped region along the diagonals, the conformal factor varies only little, from which its usefulness for geography is derived: The continents on the Earth are situated in such a way that they lie roughly in the regions of low variability of the conformal factor, leading to a faithful representation of the relative size of geographic features. Regions of high variability of the conformal factor are found on the open oceans, where they would not matter visually. A funky side effect of this is that Australia and New Zealand are projected onto two different lobes and appear to be far away from each other. But when tiling the maps they again assume a sensible separation relative to each other.

In general, the projected shapes of meridians and circles of latitude are complicated, but there are two perfectly straight meridians running from North to South pole along the diagonals of Peirce's projection, and the circles of latitude are assume more circular projected shapes close to the poles, while approximating the lozenge-shaped form of the equator at low latitude, as shown in Fig. 2. Due to the conformality of the mapping, they always intersect at right angles. The inverse mapping of a checker pattern in Peirce's domain back to the sphere shows that there are four points, where the conformal factor becomes zero.

Fig. 3 illustrates two key results at the same time, with the Earth as a well-known example: First, it shows how the entire surface gets projected onto the square according to Peirce's quincuncial projection. Second, it shows how the spherical harmonics analyse all features of the function $\psi(\theta, \varphi)$, here topographical height, as a function of scale $\lambda = \pi/\ell$ (in radians) in evaluating the transformation eqn. (4).

When assembling $\psi(\theta, \varphi)$ from $\psi_{\ell m}$ according to eqn. (5), information on successively smaller and smaller scales is added, such that finer and finer geographical details are visible. A rough estimate can make this more qualitative: $\ell = 100$ corresponds to features of size $\lambda = \pi/100$, i.e. $\sim 2^\circ$. With 60 arcminutes in a degree, one arcminute being the angle subtended by a nautical mile on the surface of the Earth,

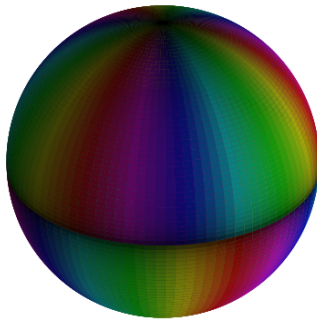
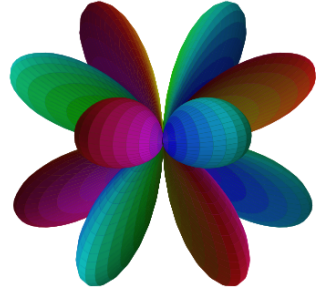
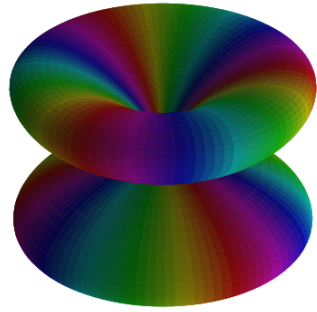


Figure 1. Spherical harmonic $Y_{43}(\theta, \varphi)$ as an absolute value $|Y_{43}(\theta, \varphi)|$ (top), real value $\text{Re } Y_{43}(\theta, \varphi)$ (centre) and on the unit sphere (bottom), all with the phase $\exp(im\varphi)$ as colouring.

and the conversion of 1852 meters per nautical mile these

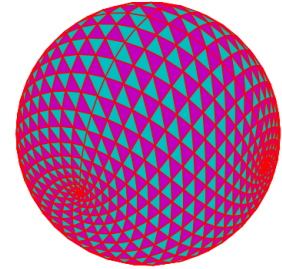
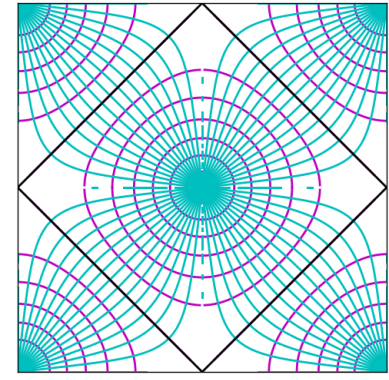


Figure 2. The mapping of meridians and circles of latitude on a 6° -graticule in azimuth and a 15° -graticule in polar angle in Peirce's projection onto a square. The black diamond-shaped line indicates the equator (top). The inverse mapping of a Cartesian grid on Peirce's domain back onto the sphere. There are four points on the equator (two are visible in the front and two on the far side of the sphere) where the conformal factor becomes zero (bottom).

particular features are of size ~ 200 km, so continents are clearly visible. Topographical details like mountain ranges or the Mediterranean Sea are resolved, but for individual islands in the Caribbean Sea or in the Mediterranean ℓ_{\max} would need to be larger still.

The implementation by [Fong \(2010, 2024\)](#) that computes spherical coordinates (θ, φ) from quincuncial coordinates (x, y) in the domain $[-1, +1] \otimes [-1, +1]$ forms the basis of this article. Explicit conversion formulas are given in the Appendix. The inverse projection is given by [Solanilla et al \(2016\)](#).

3.1. Zonal, sectoral and tesseral $Y_{\ell m}(\theta, \varphi)$

The spherical harmonics can be classified according to the value of m for a given ℓ , as they do change their character perceptibly depending on m : This classification has as categories zonal ($m = 0$), sectoral ($\ell = +m$ or $\ell = -m$) and tesseral in all other cases. The zonal $Y_{\ell 0}(\theta, \varphi)$ are real valued, as the term $\exp(im\varphi)$ as the only source of complex values, is inactive for $m = 0$, and they are necessarily azimuthally symmetric, because of the same reason. This behaviour is shown in Fig. 4, where the spherical harmonic $Y_{40}(\theta, \varphi)$ is shown in a 3d representation and as a 2d Peirce's projection. One clearly sees the lobes at the North and South

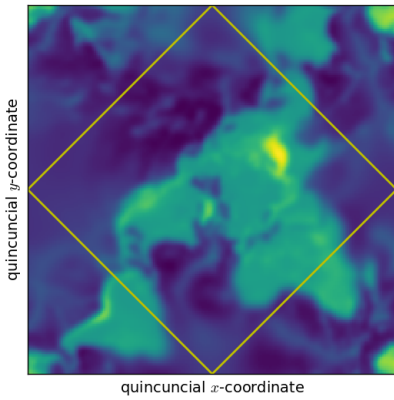


Figure 3. The Earth in Peirce's quincuncial projection, generated as a topographical map from the superposition of spherical harmonics, up to $\ell_{\max} = 100$. The yellow diamond shape is the equator in Peirce's projection. The map is smoothed with a Gaussian filter, for suppressing diffraction-like artefacts.

pole with equal sign, the equatorial bulge with the same sign, and the two rings at intermediate Northern and Southern latitudes.

The sectoral spherical harmonic $Y_{44}(\theta, \varphi)$ is depicted in Fig. 5: Its functional values on the North and South pole are zero, and large amplitudes appear on the equator. As $m = 4$, the complex phase cycles through the interval $0 \dots 2\pi$ exactly four times, and the real value exhibits four positive maxima and four negative minima.

Finally, the tesseral spherical harmonics $Y_{\ell m}(\theta, \varphi)$ where $m \neq 0$ and $|m| \neq \ell$ are shown in Fig. 6, specifically $Y_{41}(\theta, \varphi)$, $Y_{42}(\theta, \varphi)$ and $Y_{43}(\theta, \varphi)$. As soon as $\ell + m$ is odd, the associated Legendre-polynomials $P_{\ell m}(\cos \theta)$ assume a value of zero at the equator, which in Peirce's projection is mapped onto a diamond shape. The value of m determines as well, how often the complex phase cycles through the interval $0 \dots 2\pi$: In consequence, one should see each colour m times on a ring of constant latitude, and $2m$ orbitals in the 3d projection of the real value of $Y_{\ell m}$, m with a positive sign and m with a negative sign.

Fig. 7 shows the spherical harmonic $Y_{\ell m}(\theta, \varphi)$ for the choice $\ell = 11$ and $m = 3$. Clearly, the associated Legendre-polynomials in $\cos \theta$ show 10 zeros between North and South pole, and each color appears three times in azimuth. The subsequent bulges of the associated Legendre-polynomials differ in sign, which is equivalent to a phase shift of π : This can be seen in the alternating colour gradients. In fact, the phase variation in azimuth is identical in every second bulge, due to $(-1)^2 = 1$.

3.2. Visualisation of particular properties of $Y_{\ell m}(\theta, \varphi)$

3.2.1. Hermiticity

Spherical harmonics as complex valued functions have simple behaviour under complex conjugation,

$$Y_{\ell m}^*(\theta, \varphi) = (-1)^m Y_{\ell, -m}(\theta, \varphi), \quad (8)$$

where one needs to change the sign of m and add a prefactor $(-1)^m$ to form the Hermiticity condition shown in Fig. 8: It compares $Y_{3,+1}^*(\theta, \varphi)$ and $Y_{3,-1}(\theta, \varphi)$ side by side, where the factor $(-1)^1 = -1$ relates the two: The places at which the colours appear are shifted in azimuthal angle φ by π .

3.2.2. Parity

The values of a spherical harmonic at coordinates θ, φ and the antipodal point $\pi - \theta, \varphi + \pi$ are related by a prefactor of $(-1)^\ell$,

$$Y_{\ell m}(\pi - \theta, \varphi + \pi) = (-1)^\ell Y_{\ell m}(\theta, \varphi). \quad (9)$$

This behaviour under parity transform is illustrated in Fig. 9, where $Y_{32}(\pi - \theta, \varphi + \pi)$ and $Y_{32}(\theta, \varphi)$ are shown side by side. As $\ell = 3$, the prefactor relating the two functions is $(-1)^3 = -1$. It is striking to see that this prefactor shifts the colours, which repeat twice on each ring of constant latitude, by $\pi/2$ in azimuth.

3.2.3. Orthonormality

The orthonormality condition of the spherical harmonics reads

$$\int_{4\pi} d\Omega Y_{\ell m}(\theta, \varphi) Y_{\ell' m'}^*(\theta, \varphi) = \delta_{\ell\ell'} \delta_{mm'}, \quad (10)$$

and reflects that the integral over the solid angle $d\Omega = \sin \theta d\theta d\varphi$ of a pair of functions, one of which is complex conjugated, is a Hermitean scalar product. If one of the index pairs contains two unequal indices, the integral should yield zero, because the integrand shows a complete cancellation over the surface of the sphere. This is illustrated in Fig. 10, where the absolute value as a function of θ and φ is symmetric when comparing the Northern and the Southern hemisphere, and the phase varies smoothly between 0 and 2π in the azimuthal direction, leading to a vanishing integral.

3.2.4. Completeness

The completeness relation,

$$\delta_D(\cos \theta - \cos \theta') \delta_D(\varphi - \varphi') = \sum_{\ell=0}^{\infty} \sum_{m=-\ell}^{+\ell} Y_{\ell m}(\theta, \varphi) Y_{\ell m}^*(\theta', \varphi'), \quad (11)$$

states that there is a representation of the Dirac δ_D -function in terms of the basis system. The cosines in the argument of the first term appear because the δ_D -functions are normalised with respect to $d\Omega = \sin \theta d\theta d\varphi = d \cos \theta d\varphi$ as the integration measure.

For visualisation, as exemplified in Fig. 11, we choose $\cos \theta' = 1$ and $\varphi' = 0$, such that the Dirac δ_D -function should appear on the North pole. Then, the completeness relation simplifies tremendously,

$$\delta_D(\cos \theta - 1) \delta_D(\varphi) = \sum_{\ell=0}^{\infty} \sqrt{\frac{2\ell+1}{4\pi}} \sum_{m=-\ell}^{+\ell} \sqrt{\frac{(\ell-m)!}{(\ell+m)!}} Y_{\ell m}(\theta, \varphi), \quad (12)$$

because $Y_{\ell m}^*(\theta', \varphi') \propto P_{\ell m}(\cos \theta') \exp(im\varphi') = 1$, leaving only the prefactor. As expected, there is constructive interference at the North pole, and destructive interference elsewhere, and because one always adds pairs of spherical harmonics at positive and the corresponding negative m , the result is real-valued.

The gradual build-up of the Dirac function at the North pole is shown in Fig. 11 for partial sums in ℓ_{\max} . At the same

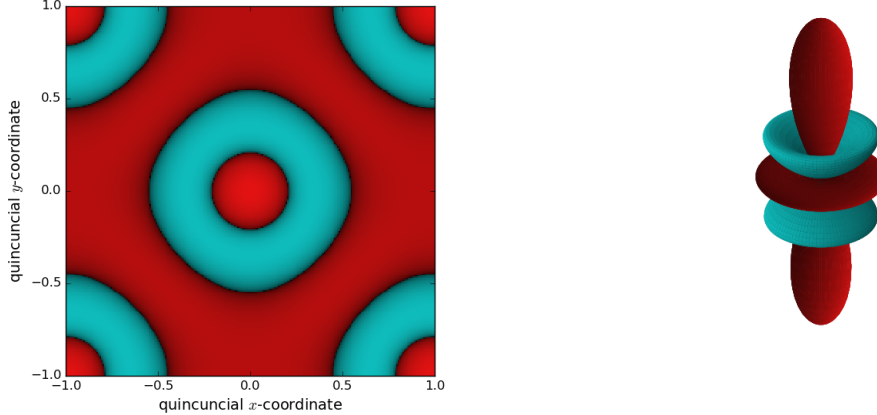


Figure 4. Zonal spherical harmonic $Y_{40}(\theta, \varphi)$, for $\ell = 4$ and $m = 0$, in a representation with $3d$ orbitals (right) and in comparison with Peirce's projection (left).

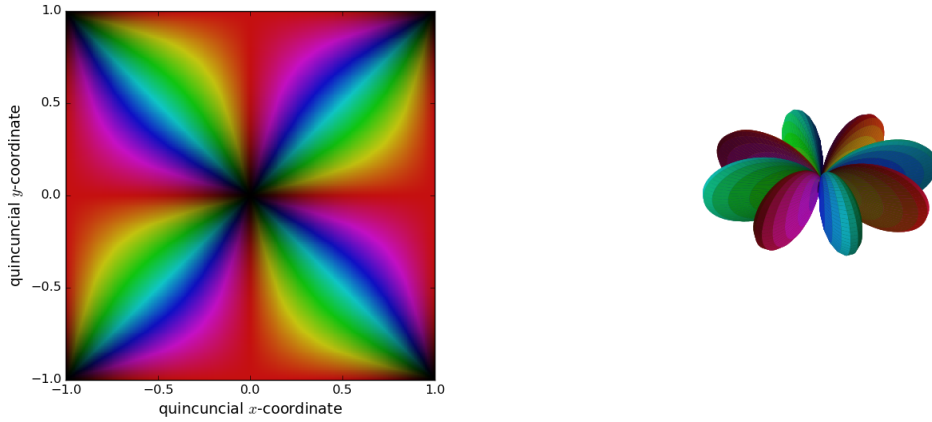


Figure 5. Sectoral spherical harmonic $Y_{44}(\theta, \varphi)$, for $\ell = m = 4$, in a representation with $3d$ orbitals (right) and in comparison with Peirce's projection (left). In both cases, colouring indicates complex phase.

time, one sees an increasing number of rings as ℓ_{\max} becomes larger, due to the more violent oscillatory behaviour of the Legendre polynomials.

3.2.5. Herglotz's generating function

Herglotz's generating function is a way to generate the spherical harmonics through a differentiation process: A plane wave

$$\exp(a_i x^i) = \sqrt{4\pi} \sum_{\ell=0}^{\infty} \sum_{m=-\ell}^{+\ell} \frac{\lambda^m r^\ell Y_{\ell m}(\theta, \varphi)}{\sqrt{(2\ell+1)(\ell+m)!(\ell-m)!}} \quad (13)$$

is explained as a sum over spherical harmonics, where the wave has a wave vector a_i and the coordinate x^i ,

$$a_i = \left(\frac{1}{2\lambda} - \frac{\lambda}{2}, -\frac{i}{2\lambda} - \frac{i\lambda}{2}, 1 \right) \quad \text{and} \quad x^i = r \begin{pmatrix} \sin \theta \cos \varphi \\ \sin \theta \sin \varphi \\ \cos \theta \end{pmatrix}. \quad (14)$$

The wave vector is peculiar as it has a norm of zero. For

simplification, we focus on the choice $\lambda = 1$, which leads to

$$\exp(a_i x^i) = \sqrt{4\pi} \sum_{\ell=0}^{\infty} \sum_{m=-\ell}^{+\ell} \frac{r^\ell Y_{\ell m}(\theta, \varphi)}{\sqrt{(2\ell+1)(\ell+m)!(\ell-m)!}} \quad (15)$$

with

$$a_i = (0, -i, 1) \quad (16)$$

such that

$$a_i x^i = r(-i \sin \theta \sin \varphi + \cos \theta), \quad (17)$$

yielding

$$\begin{aligned} \exp(a_i x^i) &= \\ &\exp(r(-i \sin \theta \sin \varphi + \cos \theta)) = \\ &\exp(-ir \sin \theta \sin \varphi) \exp(r \cos \theta). \end{aligned} \quad (18)$$

Of particular interest is the value $\theta = \pi/2$, at which $\sin \theta = 1$ and $\cos \theta = 0$. Then, $\exp(a_i x^i) = \exp(-ir \sin \varphi) = \cos(r \sin \varphi) - i \sin(r \sin \varphi)$: Consequently, one would expect this functional dependence on the equator.

The convergence of partial sums in ℓ towards the target $\exp(r(-i \sin \theta \sin \varphi + \cos \theta))$ is shown in Fig. 12, for different

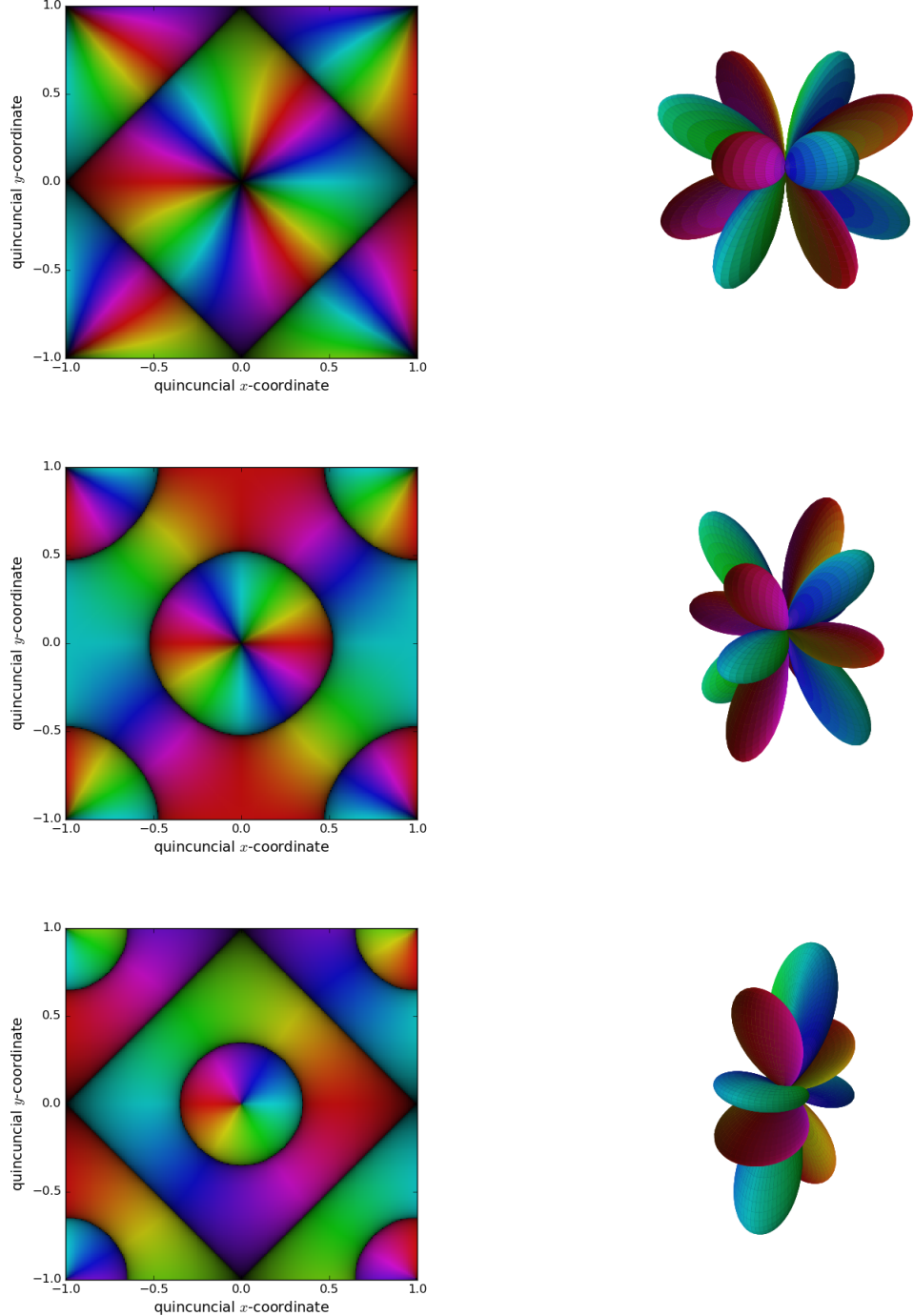


Figure 6. Tesseral spherical harmonics $Y_{\ell m}(\theta, \varphi)$, for $\ell = 4$, in a representation with $3d$ orbitals (left) and in comparison with Peirce's projection (right). In both panels, colouring indicates complex phase, for $m = 3$ (top row), $m = 2$ (centre row) and $m = 1$ (bottom row).

values of ℓ_{\max} . The features around the North pole present at low ℓ_{\max} vanish rather quickly with increasing ℓ_{\max} .

3.2.6. Rayleigh-expansion

The Rayleigh-expansion states that there is a superposition of spherical waves that gives rise to a plane wave,

$$\exp(ik_i r^i) = 4\pi \sum_{\ell=0}^{\infty} i^{\ell} j_{\ell}(kr) \sum_{m=-\ell}^{+\ell} Y_{\ell m}(\hat{r}) Y_{\ell m}^*(\hat{k}), \quad (19)$$

which plays a role in the partial wave decomposition technique in scattering theory and in cosmology, particularly in applications such as $3d$ weak gravitational lensing (Heavens 2003).

While such a relation might appear surprising at first sight, it is readily explained by the fact that Euclidean space has both shifts and rotations as fundamental symmetries. \hat{r} and \hat{k} are shorthand notations of unit vectors associated with r^i and k_i . Having the wave propagate into the z -direction

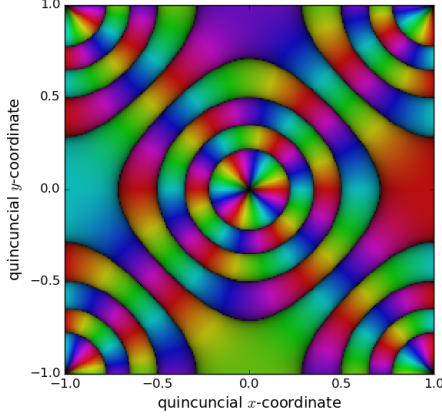


Figure 7. Spherical harmonic $Y_{11,3}(\theta, \varphi)$, with $\ell = 11$ and $m = 3$.

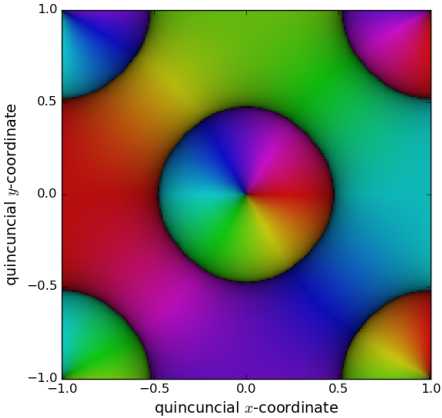
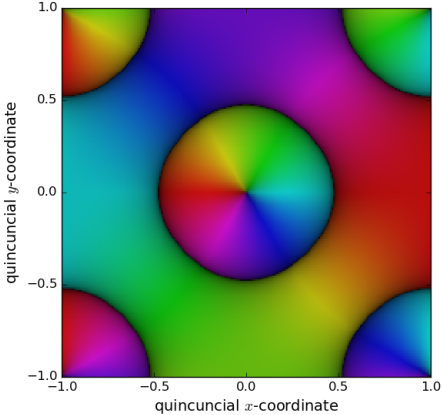


Figure 8. Spherical harmonic $Y_{\ell m}^*(\theta, \varphi)$ (top) and in comparison $Y_{\ell, -m}(\theta, \varphi)$ (bottom), for $\ell = 3$ and $m = 1$. The two plots differ by a factor $(-1)^m = -1$, illustrating the hermiticity relation.

with a unit wave vector $k_i = (0, 0, 1)$ gives $k_i r^i = r \cos \theta$, implying

$$4\pi \sum_{\ell=0}^{\infty} i^{\ell} j_{\ell}(kr) \sum_{m=-\ell}^{+\ell} Y_{\ell m}(\hat{r}) Y_{\ell m}^*(\hat{k}) = \exp(ir \cos \theta), \quad (20)$$

if r^i has the norm $r_i r^i = r^2$.

Fig. 13 demonstrates that cumulative evaluations of

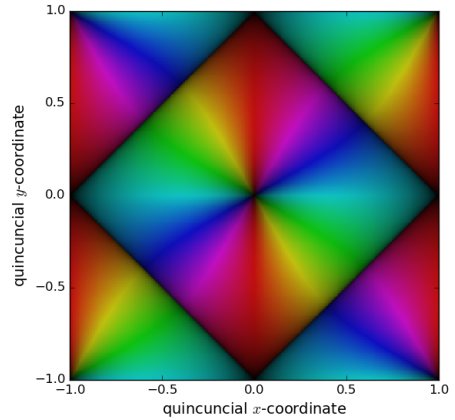
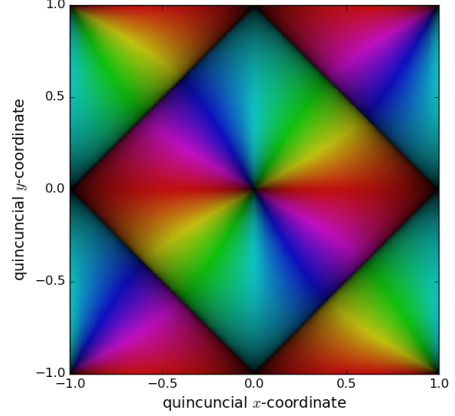


Figure 9. Spherical harmonic $Y_{\ell m}(\pi - \theta, \varphi + \pi)$ (top) and in comparison $Y_{\ell m}(\theta, \varphi)$ (bottom), for $\ell = 3$ and $m = 2$. The two plots differ by a factor $(-1)^{\ell} = -1$, showing the influence of parity inversion.

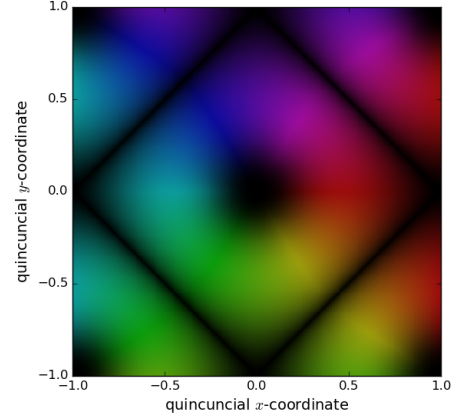


Figure 10. Product $Y_{\ell m}(\theta, \varphi) Y_{\ell' m'}^*(\theta, \varphi)$ for $\ell, m = 4, 3$ and $\ell', m' = 5, 4$, for illustration of the orthonormality relation.

eqn. (19) approximate the plane wave better with increasing ℓ_{\max} . Convergence is surprisingly fast, and already at low ℓ_{\max} one approximates the final plane wave remarkably well.

3.2.7. Wigner 3j-symbols

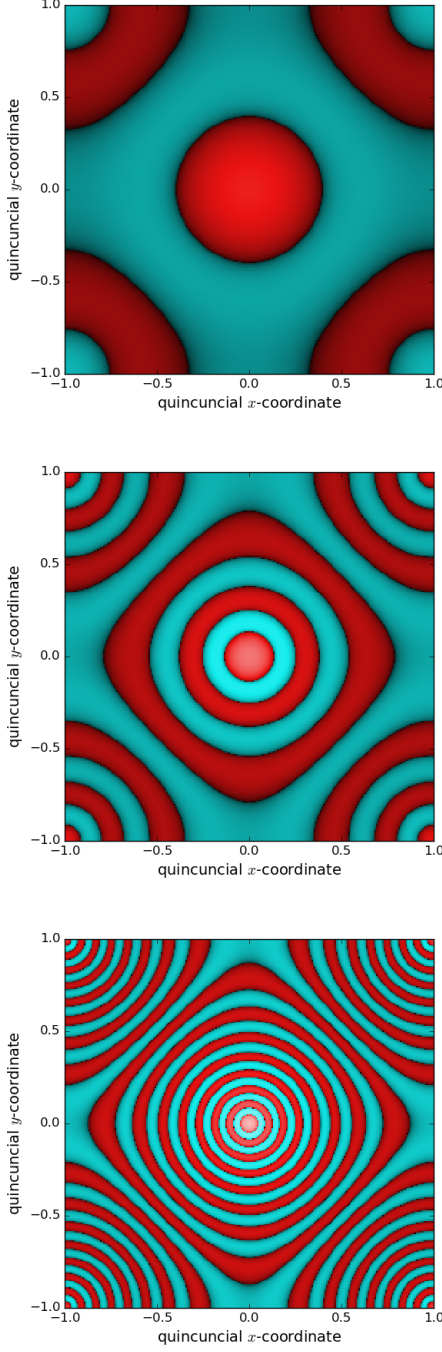


Figure 11. Partial sums in ℓ of the completeness relation, for $\theta' = 0 = \varphi'$: In consequence, the δ_D -function should appear at the North pole at the centre of the plot, successively approximated as $\ell_{\max} = 3$ (first panel), $\ell_{\max} = 10$ (second panel), $\ell_{\max} = 30$ (third panel).

While the integral over two spherical harmonics is simply the orthonormality relation, the integral over a product of

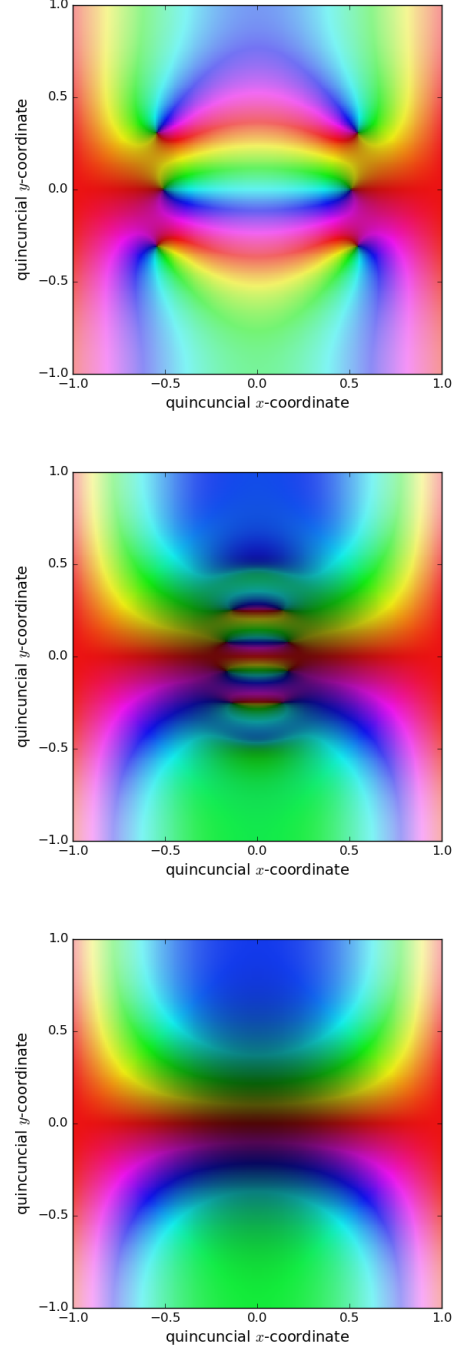


Figure 12. Herglotz's generating function, shown as partial sums in ℓ , and the target function $\exp(-ir \sin \theta \sin \varphi + r \cos \theta)$ for the particular choice $\lambda = 1$ (third panel), shown for $\ell_{\max} = 3$ (first panel), $\ell_{\max} = 10$ (second panel), all for the choice $r = 4$.

three spherical harmonics

$$\int_{4\pi} d\Omega Y_{\ell_1 m_1}(\theta, \varphi) Y_{\ell_2 m_2}(\theta, \varphi) Y_{\ell_3 m_3}(\theta, \varphi) = \sqrt{\frac{(2\ell_1 + 1)(2\ell_2 + 1)(2\ell_3 + 1)}{4\pi}} \begin{pmatrix} \ell_1 & \ell_2 & \ell_3 \\ 0 & 0 & 0 \end{pmatrix} \begin{pmatrix} \ell_1 & \ell_2 & \ell_3 \\ m_1 & m_2 & m_3 \end{pmatrix} \quad (21)$$

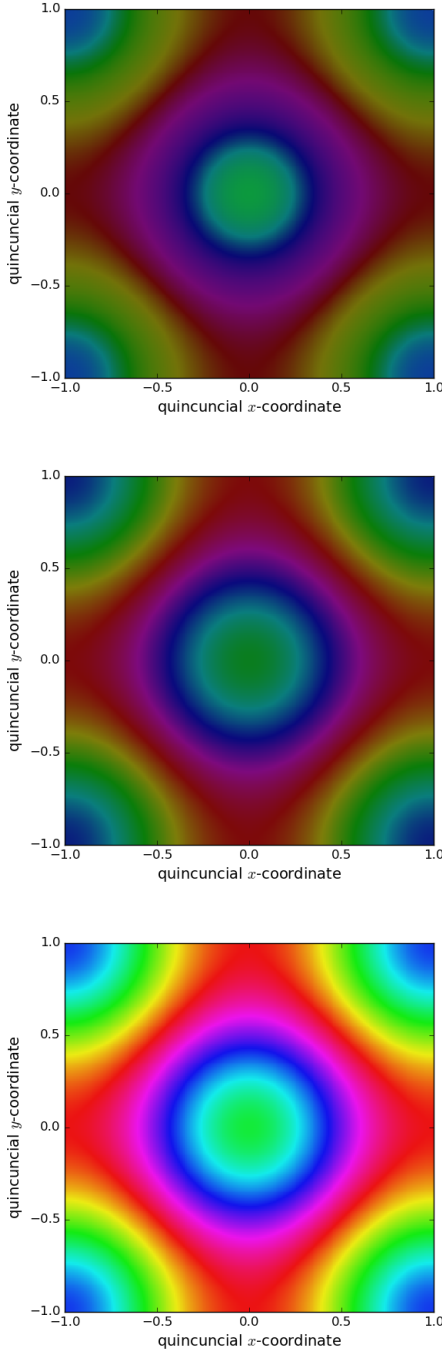


Figure 13. Partial sums in ℓ for Rayleigh's expansion, which should successively give rise to $\exp(i\varphi \cos \theta)$ (third panel), shown for $\ell_{\max} = 3$ (first panel), $\ell_{\max} = 10$ (second panel), all for the choice $r = 4$.

gives rise to the Wigner-3j symbols: There are closed forms for evaluation, but more importantly, there are straightforward rules under what circumstances the right hand side of eqn. (21) can at all be unequal to zero: The sum of all m_i needs to vanish, $m_1 + m_2 + m_3 = 0$, the ℓ_i need to fulfil the triangle inequality, $|\ell_1 - \ell_2| \leq \ell_3 \leq \ell_1 + \ell_2$, and the sum of all ℓ_i , $\ell_1 + \ell_2 + \ell_3$, needs to be an even integer.

Fig. 14 shows three cases where these conditions are individually violated, such that the integral in eqn. (21) vanishes. The first case, where $m_1 + m_2 + m_3 = 1$ instead of zero, gives

rise to a complex valued function $\propto \exp(i\varphi)$ with a single cycle through the colours. Consequently, one finds a cancellation of all contributions to the integral at φ and $\varphi + \pi$. The second case deals with a violation of the triangle inequality, as $\ell_3 = 5$ does not fulfil $|\ell_1 - \ell_2| \leq \ell_3 \leq \ell_1 + \ell_2$ with $\ell_1 = 1$ and $\ell_2 = 2$. The sum of all m is zero, such that the integrand is real-valued, and with similar areas of opposite signs one can guess the integration to vanish. A clearer case is the third, where the sum $\ell_1 + \ell_2 + \ell_3 = 5$ is odd instead of even, and the visualisation shows a Northern hemisphere with opposite sign to the Southern hemisphere, again leading to a zero result.

3.2.8. Recovery of Fourier-transforms in the small-angle limit

On small scales, the spherical harmonics $Y_{\ell m}(\theta, \varphi)$ should approximate plane waves at high ℓ , as can be seen by this argument: The actual defining differential equation

$$\Delta Y_{\ell m}(\theta, \varphi) = -\ell(\ell + 1)Y_{\ell m}(\theta, \varphi) \quad (22)$$

transitions to

$$\Delta Y_{\ell m}(\theta, \varphi) = -\ell^2 Y_{\ell m}(\theta, \varphi), \quad \text{for } \ell \gg 1 \quad (23)$$

in recovery of the Helmholtz differential equation which has plane waves as solutions, with wave number ℓ . Intuitively, this means that on small scales $\theta \ll \pi$, that are probed when $\ell \gg 1/\pi$, the curvature of the sphere can be neglected and the sphere can be locally approximated by a tangential plane. On that plane, the harmonic decomposition eqn. (4) falls back onto a Fourier-transform. While plane waves are a part of the $Y_{\ell m}(\theta, \varphi)$ in the φ -direction for any index, the Legendre polynomials are well approximated by sinusoidal waves for $\ell \gg 1$, as their amplitudes become constant and their zeros equidistant.

This is shown in Fig. 15 for the combination $\ell = 40$ and $m = 30$. Typical wave lengths amount to a few degrees, and one sees the checkered pattern generated by this tesseral spherical harmonic. At the same time, one clearly sees how Peirce's projection has relatively small distortions along the diagonals, but relatively strong distortions at the centres of the sides, where the checker pattern appears enlarged.

3.2.9. Unitary time evolution in quantum mechanics

Time evolution of wave functions in quantum mechanics is accomplished by a unitary operator $U(t, t_0)$,

$$U(t, t_0) = \exp\left(-\frac{2\pi i H(t - t_0)}{\hbar}\right) \quad (24)$$

acting on the wave function

$$\psi(t) = U(t, t_0)\psi(t_0), \quad (25)$$

with Planck's constant \hbar and the Hamilton-operator H . If the system is in an energy eigenstate, the phase of the wave function evolves linearly with time by virtue of $U(t, t_0)$. Unitary time-evolution applied to $Y_{77}(\theta, \varphi)$ shows a smooth flow of the colours in azimuth. The (stationary) probability current associated with this phase evolution gives rise to the magnetic moment, which could be measured in e.g. a hydrogen atom with the quantum number $m = 7$.

4. SUMMARY

Peirce's quincuncial projection allows visualisations of functions defined on the surface of the sphere, in particular

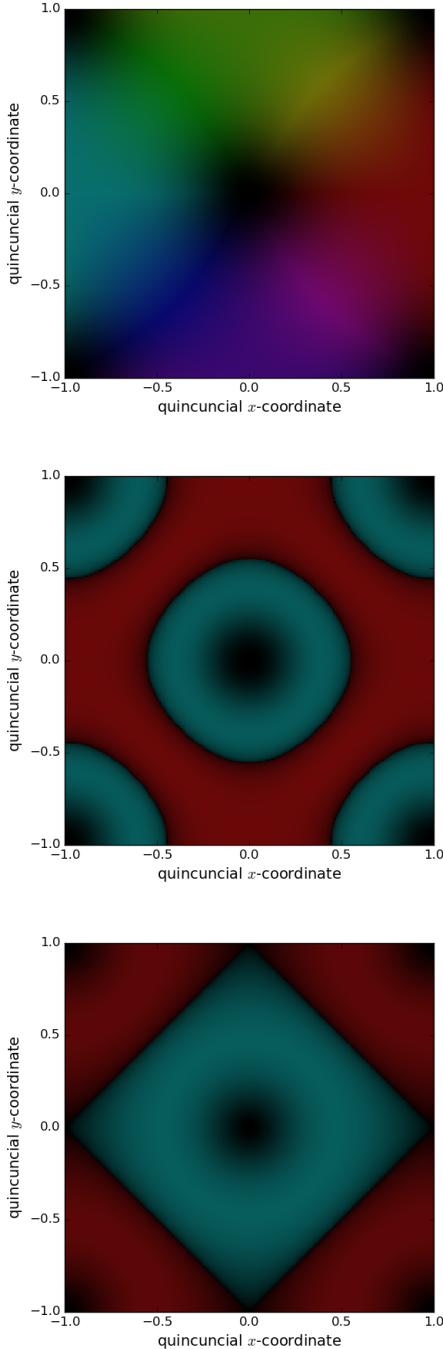


Figure 14. Product of three spherical harmonics, where the choice $Y_{11}(\theta, \varphi)Y_{22}(\theta, \varphi)Y_{2,-2}(\theta, \varphi)$ in the first panel violates the condition $m_1 + m_2 + m_3 = 0$, with the choice $Y_{11}(\theta, \varphi)Y_{22}(\theta, \varphi)Y_{5,-3}(\theta, \varphi)$ in the second panel in contradiction with the triangle inequality, and for the case $Y_{11}(\theta, \varphi)Y_{21}(\theta, \varphi)Y_{2,-2}(\theta, \varphi)$, where the sum $\ell_1 + \ell_2 + \ell_3$ is odd instead of even.

of the spherical harmonics $Y_{\ell m}(\theta, \varphi)$, which find widespread use in physics, geophysics and astronomy. In particular the complex structure of the $Y_{\ell m}(\theta, \varphi)$ and their symmetries can be illustrated, in conjunction with their fundamental properties that make them attractive for usage throughout physics: (i) hermiticity, (ii) parity, (iii) orthonormality, (iv) completeness, (v) Herglotz's generating function, (vi) the Rayleigh expansion of plane waves into spherical waves,

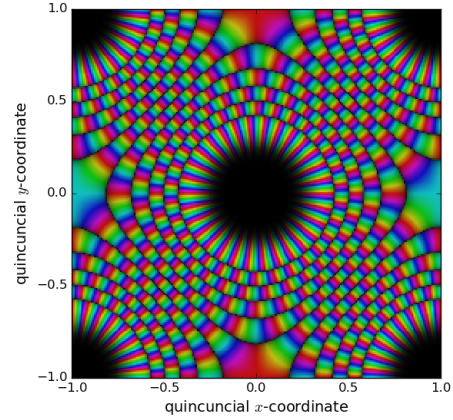


Figure 15. Spherical harmonics $Y_{\ell m}(\theta, \varphi)$ for very high $\ell = 40$, where the small angle approximation is applicable, for a choice of $m = 30$ corresponding to the tesseral type. At the centres of the sides of the map one clearly sees the distortion induced by the variability of the conformal factor.

(vii) the Wigner 3j-symbols and finally (viii) their relation to Fourier-transforms. There are advantages of representing the spherical harmonics in a flat map projection in some cases, and it makes their functional form accessible to students who find it difficult to visualise 3d-structures.

5. ACKNOWLEDGEMENTS

I thank Chamberlain Fong for encouragement to write this article. The *python*-scripts used for generating the plots are available on request from the author. I acknowledge the implementation of the quincuncial projection by C. Fong ([Fong 2010, 2024](#)), which I translated from *matlab* to *python*. Visualisations of the phase of complex function by colour are difficult to process by readers with a divergent colour perception: I am working on plotting scripts in *python* for complex functions that use a perceptually uniform colormap. Numerical implementations for Jacobi's elliptical functions were the ones in *SciPy*, and for the spherical harmonics I used the *python* package *Spheroidal*. The data set of the spherical harmonics expansion coefficients of the Earth was kindly provided by Matthias Bartelmann, and I thank Tristan Bereau for comments on the topological map. I am grateful to Theodora Lazarevic and Justus Zimmermann for spotting mistakes.

REFERENCES

- Adamek J, Durrer R, Tansella V (2015) Lensing signals from spin-2 perturbations. [arxiv/151001566](http://arxiv.org/abs/1510.01566) URL <http://arxiv.org/abs/1510.01566>, 1510.01566
- Beck D, Fabbian G, Errard J (2018) Lensing reconstruction in post-born cosmic microwave background weak lensing. [arxiv/180601216](http://arxiv.org/abs/1806.01216) URL <http://arxiv.org/abs/1806.01216>, 1806.01216
- Christoffel EB (1867) Sul problema delle temperature stazionarie e la rappresentazione di una data superficie. DOI 10.1007/bf02419161, URL <https://doi.org/10.1007/bf02419161>
- Dray T (1985) The relationship between monopole harmonics and spin-weighted spherical harmonics. *Journal of Mathematical Physics* 26(5):1030–1033, DOI 10.1063/1.526533, URL <https://doi.org/10.1063/1.526533>, https://pubs.aip.org/aip/jmp/article-pdf/26/5/1030/19220480/1030_1_online.pdf
- Driscoll TA, Trefethen LN (2002) Schwarz-Christoffel Mapping. Cambridge Monographs on Applied and Computational Mathematics, Cambridge University Press

Fernández-Cobos R, Marcos-Caballero A, Vielva P, Martínez-González E, Barreiro RB (2016) Exploring 2-spin internal linear combinations for the recovery of the CMB polarization. arxiv/160101515 URL <http://arxiv.org/abs/1601.01515>, 1601.01515

Fong C (2010) Warping pierce quincuncial panoramas. CoRR abs/1011.3189, URL <http://arxiv.org/abs/1011.3189>, 1011.3189

Fong C (2024) Analytical methods for squaring the disc. URL <https://arxiv.org/abs/1509.06344>, 1509.06344

Gluscevic V, Kamionkowski M, Cooray A (2009) De-rotation of the cosmic microwave background polarization: Full-sky formalism. Physical Review D 80(2), DOI 10.1103/PhysRevD.80.023510, URL <http://arxiv.org/abs/0905.1687>, 0905.1687

Goldberg JN, Macfarlane AJ, Newman ET, Rohrlich F, Sudarshan ECG (1967) Spin-s spherical harmonics and δ . Journal of Mathematical Physics 8(11):2155–2161, DOI 10.1063/1.1705135, URL <http://aip.scitation.org/doi/abs/10.1063/1.1705135>

Gorski KM, Wandelt BD, Hansen FK, Hivon E, Banday AJ (1999) The healpix primer. URL <https://arxiv.org/abs/astro-ph/9905275>, astro-ph/9905275

Gorski KM, Hivon E, Banday AJ, Wandelt BD, Hansen FK, Reinecke M, Bartelmann M (2005) Healpix: A framework for high-resolution discretization and fast analysis of data distributed on the sphere. The Astrophysical Journal 622(2):759–771, DOI 10.1086/427976, URL <http://dx.doi.org/10.1086/427976>

Hall A, Taylor A (2014) Intrinsic alignments in the cross-correlation of cosmic shear and cosmic microwave background weak lensing. MNRAS 443:L119–L123, DOI 10.1093/mnrasl/slu094

Hanson D, Challinor A, Lewis A (2010) Weak lensing of the CMB. General Relativity and Gravitation 42(9):2197–2218, DOI 10.1007/s10714-010-1036-y, URL <http://link.springer.com/10.1007/s10714-010-1036-y>

Heavens A (2003) 3D weak lensing. \mnras 343:1327–1334, DOI 10.1046/j.1365-8711.2003.06780.x

Hirata CM, Seljak U (2003) Reconstruction of lensing from the cosmic microwave background polarization. Physical Review D 68(8):083,002–+

Hudson JA (1978) Physics of the earth f. d. stacey, john wiley & sons, 1977 414 pages. Geophysical Journal International 52(2):366–366, DOI 10.1093/gji/52.2.366, URL <https://doi.org/10.1093/gji/52.2.366>, <https://academic.oup.com/gji/article-pdf/52/2/366/1649642/52-2-366.pdf>

Huffenberger KM, Wandelt BD (2010) Fast and exact spin-s spherical harmonic transforms. The Astrophysical Journal Supplement Series 189(2):255, DOI 10.1088/0067-0049/189/2/255, URL <http://dx.doi.org/10.1088/0067-0049/189/2/255>

Hughes SA (2000) Evolution of circular, nonequatorial orbits of kerr black holes due to gravitational-wave emission. Phys Rev D 61:084,004, DOI 10.1103/PhysRevD.61.084004, URL <https://link.aps.org/doi/10.1103/PhysRevD.61.084004>

Kamionkowski M, Kovetz ED (2015) The quest for b modes from inflationary gravitational waves. arxiv/151006042 URL <http://arxiv.org/abs/1510.06042>, 1510.06042

Leistedt B, McEwen JD, Kitching TD, Peiris HV (2015) 3d weak lensing with spin wavelets on the ball. arxiv/150906750 URL <http://arxiv.org/abs/1509.06750>, 1509.06750

Lewis A, Challinor A (2007) The 21cm angular-power spectrum from the dark ages. Physical Review D 76(8), DOI 10.1103/PhysRevD.76.083005, URL <http://arxiv.org/abs/astro-ph/0702600>, astro-ph/0702600

Maino D, Burgana C, Maltoni M, Wandelt BD, G{\textbackslash}textbackslash orski KM, Malaspina M, Bersanelli M, Mandolcsi N, Banday AJ, Hivon E (1999) The planck-LFI instrument: Analysis of the 1/f noise and implications for the scanning strategy. AAPS 140:383–391

Merkel P, Schaefer BM (2011) Gravitational lensing of the cosmic microwave background by nonlinear structures. Monthly Notices of the Royal Astronomical Society 411(2):1067–1076, DOI 10.1111/j.1365-2966.2010.17739.x, URL <http://arxiv.org/abs/1007.1408>, 1007.1408

Nishizawa AJ, Komatsu E, Yoshida N, Takahashi R, Sugiyama N (2008) Cosmic microwave background-weak lensing correlation: Analytical and numerical study of non-linearity and implications for dark energy. The Astrophysical Journal 676(2):L93–L96, DOI 10.1086/587741, URL <http://arxiv.org/abs/0711.1696>, 0711.1696

Okamoto T, Hu W (2003) Cosmic microwave background lensing reconstruction on the full sky. Physical Review D 67(8):083,002–+, DOI 10.1103/PhysRevD.67.083002

Olver FWJ, Olde Daalhuis AB, Lozier DW, Schneider BI, Boisvert RF, Clark CW, Miller BR, Saunders BV, Cohl HS, McClain MA (2025) Nist digital library of mathematical functions. <https://dlmf.nist.gov/>, Release 1.2.4 of 2025-03-15, URL <https://dlmf.nist.gov/>

Peirce CS (1879) A quincuncial projection of the sphere. American Journal of Mathematics 2(4):394–396, URL <http://www.jstor.org/stable/2369491>

Schwarz H (1869) Über einige abbildungsaufgaben. Journal für die reine und angewandte Mathematik 1869(70):105–120, DOI doi:10.1515/crll.1869.70.105, URL <https://doi.org/10.1515/crll.1869.70.105>

Seljak U (1996) Gravitational lensing effect on cosmic microwave background anisotropies: A power spectrum approach. ApJ 463:1, DOI 10.1086/177218

Solanilla L, Oostra A, Yanez J (2016) Peirce quincuncial projection, Revista Integracion, vol 34. Escuela de Matematicas

Zaldarriaga M, Seljak U (1998) Gravitational lensing effect on cosmic microwave background polarization. Physical Review D 58(2):023,003–+, DOI 10.1103/PhysRevD.58.023003

APPENDIX

PROJECTION FORMULAS FOR PEIRCE'S QUINCUNCIAL PROJECTION

The explicit relation for projecting a point on the square domain $(x, y) \in [-1, +1] \times [-1, +1]$ to coordinates x, y the stereographic plane is given by

$$u = K(m)(x - 1) \quad \text{and} \quad w = K(m)y \quad (\text{A1})$$

with the complete elliptic integral

$$K(m) = \int_0^{\pi/2} d\vartheta \frac{1}{\sqrt{1 - m \sin^2 \vartheta}} \quad (\text{A2})$$

where we need the specific value $m = 1/2$. Furthermore, the Jacobi elliptic functions are implicitly defined through the relations

$$\text{sn}(u(\varphi), m) = \sin \varphi, \quad \text{cn}(u(\varphi), m) = \cos \varphi, \quad \text{dn}(u(\varphi), m) = \sqrt{1 - m^2 \sin^2 \varphi} \quad (\text{A3})$$

with the elliptic integral

$$u(\varphi) = \int_0^{\varphi} d\vartheta \frac{1}{\sqrt{1 - m^2 \sin^2 \vartheta}} \quad (\text{A4})$$

Then, the abbreviations

$$s = \text{sn}(u, m), \quad c = \text{cn}(u, m), \quad d = \text{dn}(u, m) \quad (\text{A5})$$

as well as

$$s_1 = \text{sn}(w, 1-m), \quad c_1 = \text{cn}(w, 1-m), \quad d_1 = \text{dn}(w, 1-m) \quad (\text{A6})$$

are used to compute

$$\delta = c_1^2 + m(ss_1)^2 \quad (\text{A7})$$

from which the stereographic coordinates follow as

$$x = \frac{cc_1}{\delta} \quad \text{and} \quad y = -\frac{ss_1 \times dd_1}{\delta}. \quad (\text{A8})$$

Inverse stereographic projection then determines latitude λ and longitude β through

$$\lambda = 2 \arctan \sqrt{x^2 + y^2} - \pi/2 \quad \text{and} \quad \beta = \arctan(y/x), \quad (\text{A9})$$

and finally, spherical coordinates with the polar angle $\theta = \pi/2 - \lambda$ and the azimuthal angle $\varphi = \beta + \pi$ follow directly.